Mechanics of C_{60} in Nanotubes

Dong Qian, Wing Kam Liu, and Rodney S. Ruoff*

Northwestern University, Department of Mechanical Engineering, Evanston, Illinois 60208

Received: May 24, 2001; In Final Form: July 13, 2001

A modeling study of C_{60} in nanotubes is presented, with focus on a new approach. We report on the elastic properties, energetics, and certain tribological issues, for C_{60} inside (*n*, *n*) nanotubes, with *n* ranging from 5 to 10. A new combined molecular dynamics/continuum approach with account of both the nonbonded and bonded interactions was used. The elastic properties of the nanotube were analytically derived on the basis of the Tersoff-Brenner potential. The derived Young's modulus is consistent with experimental values. We have computed the case where the C_{60} has zero initial velocity and is "sucked" into the (10, 10) or (9, 9) tubes due to the sharp force gradient present from the deep attractive potential at the tube inlet; C_{60} then oscillates back and forth inside the (10, 10) and (9, 9) nanotubes. C_{60} seems to make a perfect nanobearing system when in the (10, 10) tube. In a separate modeling study, C_{60} was fired on axis at high velocity (from 400 up to 1600 m/s) toward the six different armchair nanotubes. Over this velocity range the C_{60} could only penetrate into the (10, 10) and (9, 9) nanotubes, rebounding from the (8, 8), (7, 7), (6, 6), and (5, 5) tubes.

Introduction

Fullerenes inside nanotubes have been experimentally observed. Smith et al.[1−3] and Burteaux et al.[4] used pulsed laser evaporation (PLV) of a graphite target containing a catalyst, while Sloan et al.[5] and Zhang et al.[6] used arc vaporization of carbon with a mixed Ni/Y catalyst. In addition, Sloan et al.[7] have shown that single-walled nanotubes can be selectively opened and filled with various materials using wet chemistry techniques. Nanotubes having fullerenes inside them could have different physical properties compared to empty nanotubes. Such peapod types of structures may find use in functional nanoscale devices such as nano-pistons, nano-bearings, nano-writing implements, or as a nano-capsule storage system. A recent example of a nano-bearing system involving sliding of neighboring shells in MWCNTs has been recently discovered by Yu et al.[8] and separately by Cumings et al.[9]

Treating the mechanics of fullerenes inside nanotubes involves modeling both the nonbonded interaction between the fullerene and the nanotube and the covalent bonding interactions. A new combined molecular dynamics/continuum approach is employed below with proper account of these two factors. One can also extend this approach for the analysis of nano-devices having different length scales present. Among other factors, of interest are the geometries that these hybrid NT/fullerene systems adopt, the elastic properties and energetics, and the tribology. We address some of these issues here, including the dynamics, energetics, and possible friction forces of C_{60} inside nanotubes.

Modeling Approach

Treatment of Nonbonded Interactions. The nonbonded interaction energy is obtained by summing the corresponding interaction energy for each atom pair. Three different empirical potentials were used to treat the three configurations shown in Figure 1.

TABLE 1: LJ Parameters

parameter source	*a*	σ	y_0
LJ1 (Girifalco and Lad[10])	24.3×10^{-79} J m^6	1.42 Å	2.7
LJ2 (Girifalco[11])	32×10^{-79} J m^6	1.42 Å	2.742

The first empirical potential is the classical Lennard-Jones (LJ) potential:

$$\phi_i = \frac{A}{\sigma^6}\left[\frac{1}{2}y_0^6\frac{1}{\left(\frac{r_i}{\sigma}\right)^{12}} - \frac{1}{\left(\frac{r_i}{\sigma}\right)^6}\right] \tag{1}$$

In eq 1, $\sigma = 1.42$ Å is the C−C bond length, y_0 is a dimensionless constant, and r_i is the distance between the *i*th atom pair. A cutoff length of 10σ was used in the computation.

Two sets of parameters for the LJ potential have been used. One is from Girifalco and Lad's[10] treatment of the lattice energy of graphite. The other is from Girifalco's[11] modeling of the lattice energy of C_{60} solid. Case 3, shown in Figure 1b, has also been studied by Girifalco.[11] On the basis of local density approximation (LDA) calculations, Wang et al.[12] derived the following Morse-type potential:

$$U(r) = D_e[(1 - e^{-\beta(r-r_e)})^2 - 1] + E_r e^{-\beta' r} \tag{2}$$

where $D_e = 6.50 \times 10^{-3}$ eV is the equilibrium binding energy, $E_r = 6.94 \times 10^{-3}$ eV is the hard-core repulsion energy, $r_e = 4.05$ Å, $\beta = 1.00$/Å, and $\beta' = 4.00$/Å. The difference between these three potentials is shown in Figure 2a−c.

As Figure 2a,c show, the two LJ potentials yield much higher atomic forces in the repulsive region than the LDA potential, while in the attractive region, the LDA potential gives a much lower value of the binding energy than the two LJ potentials (Figure 2b). Table 2 shows the calculated binding energy and equilibrium distance (as defined in Figure 1a,b) for each case and each of the three potentials. The equilibrium distance is obtained by finding the minimum energy for the configurations shown in Figure 1.

* Corresponding author. E-mail address: r-ruoff@northwestern.edu.

10.1021/jp0120108 CCC: $20.00
Published on Web 10/17/2001

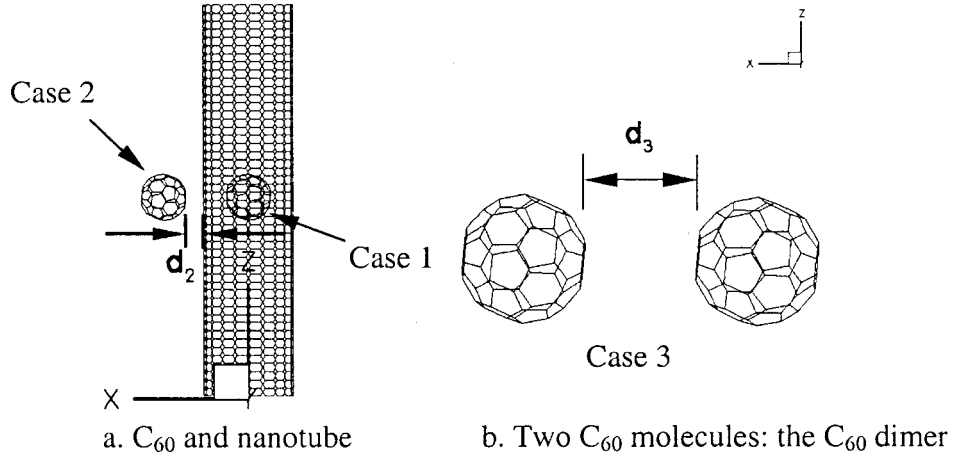

Figure 1. Configurations used in computing the binding energy. (a) C_{60} inside, and outside, the (10, 10) nanotube. (b) C_{60} dimer.

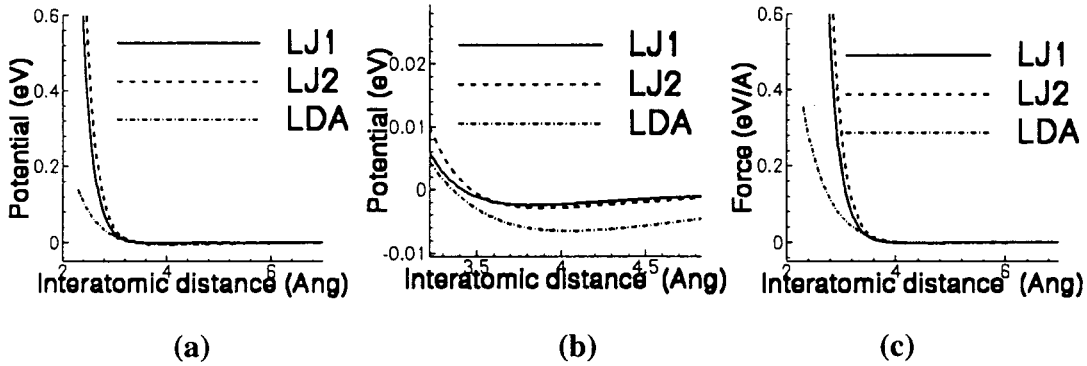

Figure 2. (a) Comparison of the three different carbon atom, atom potentials as a function of interatomic distance. (b) An expanded view of the three potentials in the attractive region. (c) Comparison of the interatomic force from the three atom, atom potentials of Figure 2a.

TABLE 2: Binding Energy and Equilibrium Separation for Different Cases

	ϕ (LJ1) (eV)	ϕ (LJ2) (eV)	ϕ (LDA) (eV)
case 1	−2.950	−3.862	−11.881
case 2	−0.488	−0.643	−2.264
case 3	−0.255	−0.317	−1.160
equilibrium distance (d_2)	2.869 Å	2.863 Å	2.465 Å
equilibrium distance (d_3)	2.742 Å	2.791 Å	2.388 Å

Due both to the more repulsive wall of the LJ potentials, and the deeper attractive well of the LDA potential, the equilibrium distance for each of the LJ potentials is much larger than that from the LDA potential.

To obtain further understanding of the repulsive wall of the LJ and LDA potentials, we computed the equation of state for the graphite system. As an approximation we treated two graphene sheets (in AA and AB registry, respectively). The in-plane geometry was held fixed, and the interlayer distance was changed. The computed pressure, as a function of the volume change, is plotted in Figure 3 along with published experimental data by Zhao et al.[13] (referred to as EXP1), and by Hanland et al.[14] (referred to as EXP2), and the ab initio treatment (which included in-plane relaxation and treated an infinite crystal) by Boettger.[15] The LDA model employed here fits this experimental data, and Boettger's model, reasonably well. The LJ1, in contrast, deviates strongly from the experimental high-pressure data for graphite (and Boettger's high-level computational treatment) when the relative volume is smaller than ∼0.9 V_0. As Figure 2b shows, the LDA model employed here is "too attractive" at distances greater than ∼3.35 Å, but it much better treats the interlayer force present in graphite for distances shorter than ∼3.0 Å. One thus needs to use the two different potentials

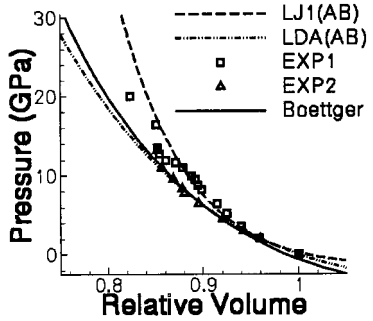

Figure 3. Comparison of the EOS for graphite using different models with experimental data.

in the regions where each well fits experimental data. Consequently, in the simulations described below, when the interatomic distance is less than 3.3 Å, the LDA potential was applied. If the interatomic distance is greater than 3.4 Å, the LJ1 potential was used. An interpolation was applied in the transition region to ensure continuity of the potential and force.

The 3D Energetic Structure. The binding energy has been calculated as a function of relative position, with the same rigid body assumption. A fine spatial grid (30 × 30 × 30) was generated around the open end of the (10,10) nanotube. The center of the C_{60} is then positioned on each node of the grid. Both the binding energy and the total force acting on the C_{60} were evaluated for each node. Shown in Figure 4a is a 3-dimensional iso-surface contour for the binding energy. To show the detail of the contour, two planes have been used. The in-plane colored contours of the binding energy are shown in Figure 4b ($x-y$ plane) and 4c ($x-z$ plane), respectively. Red denotes higher energy (repulsive) and blue denotes lower energy

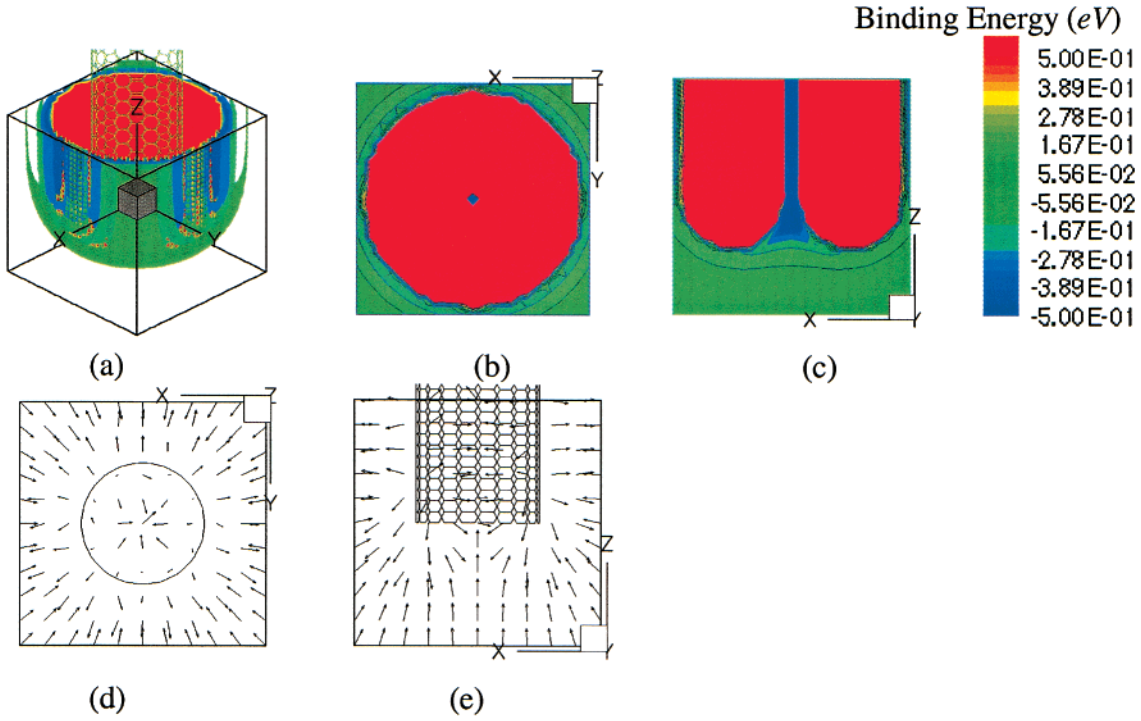

Figure 4. (a) A 3D view of the iso-surface with colored contours denoting the binding energy between C_{60} and the (10, 10) nanotube. The black cubic box shows the size of the spatial grid. The box edge length is 2 times the diameter of the (10, 10) nanotube. The center of the box is the center of the coordinate system. Two cuts show the detail of the binding energy structure. Front views of these 2 cuts are shown in (b) and (c). (b) The binding energy contour in the $x-y$ plane. (c) The binding energy contour in the $x-z$ plane. In (d) and (e) are shown the total force on C_{60} in 2 different planes: (d) the force field in the $x-y$ plane, (e) the force field in the $x-z$ plane.

(attractive). There is a minimum on the perimeter of the tube but the global minimum potential value occurs for the C_{60} inside the tube. The binding energy evaluation predicts that it is possible for C_{60}, even when initially at rest, to be pulled into the (10,10) nanotube and that the C_{60} can also be attracted to the side of the tube.

The total force on the C_{60} was computed and the corresponding force vectors are shown in Figure 4, parts d and e. The force magnitudes were found to vary significantly and for the purposes of representation all the force vectors were normalized to 1, therefore the vector field as shown only gives the direction of the interatomic force. It can be seen from Figure 4e that the repulsive force and attractive force meet on the perimeter and axis of the tube. Since all the conclusions are made on the basis of the rigid body assumption, verification by means of further simulation, including of fully relaxed fullerene and tube structures, is needed.

Bonded Interactions and Continuum Modeling

To model the bonded interaction among the carbon atoms of the nanotube, we have adapted the classical Tersoff-Brenner model.[16−17] Details about the choice of model parameters are given by Brenner.[17] A standard test of the model has been performed before the implementation. For graphite, we have obtained exactly the same values for the equilibrium distance and bonding angle reported by Brenner.[17]

The continuum treatment of the nanotube is based on the Cauchy-Born rule (Tadmor et al.,[18] Milstein[19]). The Cauchy-Born rule connects the energy for an equivalent continuum to that at the atomic scale. It assumes that each point in the continuum can be represented by the underlying crystal structure that is subjected to homogeneous deformation.

A piece of graphene sheet is shown in Figure 5. The basic element of the structure is a hexagon, with each side of the hexagon representing the sp^2 hybridized covalent bond. Since each bond is also shared by a neighboring hexagon, the total bonding energy for one hexagon can be given as half of the bond energy sum of the 6 bonds. The energy density, due to the fact that the graphene sheet results from periodic repetition of the hexagon structure, is

$$W = \frac{\Phi}{At} \tag{3}$$

where Φ is the bonding energy sum, A is the area of the undeformed hexagon, and t is the thickness of the continuum, and we used the interlayer distance of graphite.

Recall that in the theory of hyperelasticity,[20] the nominal stress $\boldsymbol{P}_{ij}$ and the first elasticity tensor $\boldsymbol{C}_{ijkl}$ are given as

$$\boldsymbol{P}_{ij} = \frac{\partial W}{\partial \boldsymbol{F}_{ji}} \tag{4}$$

and

$$\boldsymbol{C}_{ijkl} = \frac{\partial^2 W}{\partial \boldsymbol{F}_{ji} \partial \boldsymbol{F}_{lk}} \tag{5}$$

In eqs 4 and 5, $\boldsymbol{F}_{ij}$ is the deformation gradient tensor and is defined as the differentiation of the spatial coordinate $\boldsymbol{x}$ with respect to the material coordinate $\boldsymbol{X}$, i.e. $\boldsymbol{F}_{ij} = \partial x_i / \partial X_j$. Equation 5 can be used as a good approximation for estimating the mechanical properties. It can be concluded that for the equilibrium condition, the elasticity tensor has both major and minor symmetry and is isotropic. These properties can also be used as assumptions for the case of small deformation analysis. Among these features, only major symmetry holds for large deformation. By plugging in the values for all the model parameters from the Tersoff-Brenner potential, we get $C_{1111} =$

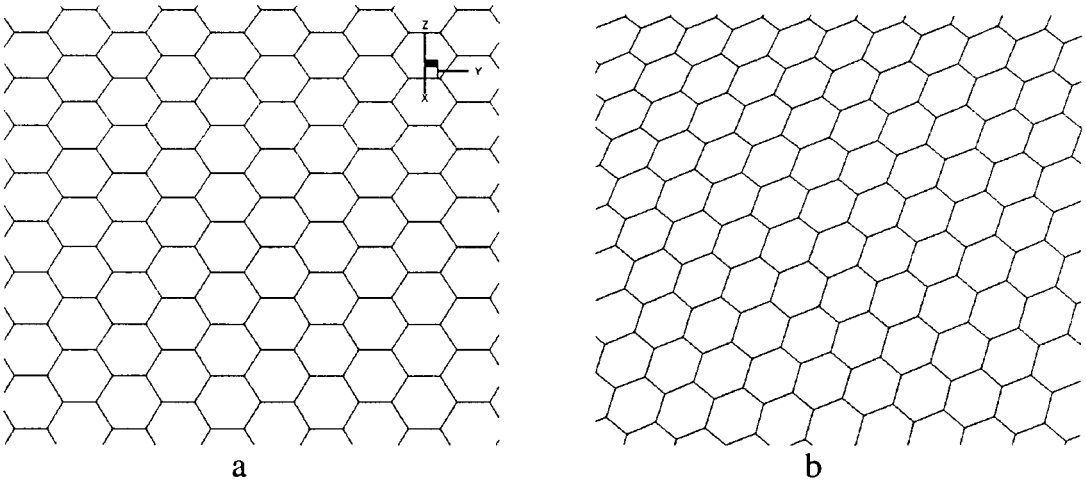

Figure 5. Crystal structure of a graphene sheet. (a) Before deformation, (b) after deformation.

$C_{2222} = 1.144$ TPa for graphite, which is close to the published data[21] (1.021216 ± 0.02 TPa). In addition, we also obtain $C_{1122} = C_{2211} = C_{1212} = C_{2121} = 0.42$ TPa, as compared to 0.18 ± 0.02 TPa given by the same publication.

Treating the graphene sheet for the plane stress case yields a Young's Modulus $E = 0.989$ TPa and Poisson's ratio $= 0.367$. The corresponding value of Young's modulus derived from publication[21] is 1.021 TPa and the Poisson's ratio $= 0.19$. The comparison implies further improvement can be made to the Tersoff-Brenner potential. Note that our approach does not depend on any bonding potential function that is used, instead, it can serve as a useful tool to check the validity of this function. The implementation of FEM/meshfree method are straightforward following eq 4. A systematic method of establishing interpolation using a meshfree scheme has been given by Liu, et al.[22] More details will be presented in a forthcoming paper.[23] For meshfree methods and applications in the analysis of shell structure, readers may consult Li, Hao and Liu,[24] Liu et al.,[25] and two special issues[26] devoted to this topic.

Results and Discussions

In the simulation, we choose the lengths of all the nanotubes to be $L = 129$ Å. The nanotubes are modeled as a cylindrical shell with thickness t. The value of t is 3.4 Å. The C_{60} is modeled directly using the Tersoff-Brenner potential. The computation is performed in a scaled system with the following ratios (superscript * denotes the scaled system): mass density $\rho^*/\rho = 1$, Young's modulus $E^*/E = 1$, length $L^*/L = 10^{10}$, time $t^*/t = 10^{10}$, energy $U^*/U = 10^{30}$, mass $m^*/m = 10^{30}$.

The time step in the scaled system is chosen as $dt^* = 5 \times 10^{-5}$, this corresponds to 5×10^{-15} s. The Verlet integration scheme has been adopted for both the continuum (the nanotube) and the molecular (the C_{60}) system. The configurations are saved every 0.5 ps. The system is first cooled to 0 K using a relaxation scheme. The following cases have been computed:

(1) C_{60} initially at rest outside, and 10 Å away on-axis, from the open end of a (10, 10) nanotube.

(2) Same as (1), but with a (9, 9) nanotube.

(3) C_{60} is initially at the same position as (1) and (2), but is fired with a finite initial velocity, on-axis toward the open ends of the (5, 5), (6, 6), (7, 7), and (8, 8) nanotubes, respectively.

Case (1) was first computed for a total time of 200 ps and 500 ps, respectively. Shown in Figure 6a is the binding energy as a function of the accumulated displacement of C_{60}. A low energy plateau is reached after 10 ps. Simulation indicates that without any external action, C_{60} was sucked into the tube from the open end. Figure 6b shows the corresponding total force components, with f_z the axial component of force. The C_{60} does not escape from the (10,10) tube, but rather is decelerated at the opposing end due to a strong restoring force. While inside the tube, the axial component of force is smaller than the force in the radial directions. The same conclusion can be inferred from Figure 6d, in which an almost constant axial velocity is observed. The C_{60} oscillates along the axis inside the nanotube, going back and forth between the two open ends, and never escapes. Moreover, the oscillation amplitude after a few cycles (Figure 6e) is almost constant and shows no sign of decay. The period of the oscillation can be estimated from the generated data and ranges between 47 and 64 ps for the (10, 10) nanotube with length of 129 Å. In addition, the forces in the x and y directions start to grow (Figure 6c) after the C_{60} is sucked back in from the opposing end. The average radius of the C_{60} was computed for each saved configuration (obtained every 0.5 ps as mentioned above). This computed average radius was always within ± 0.02 Å of the radius of an un-deformed C_{60}. On the other hand, the average radius of the (10, 10) tube (obtained every 0.5 ps) was found to be within ± 0.15 Å of the un-deformed tube radius. The (10, 10) tube was observed to have a small temperature increase (<1.8 K).

We now consider the interaction between C_{60} and the (9, 9) nanotube. In this case the C_{60} is still sucked into the tube when initially at rest. However, the radial deformation of the tube and its interaction with the C_{60} are stronger than in (10, 10), and both the binding energy and radial force components oscillate strongly. The axial component of force is larger than for the (10, 10) nanotube, and the average axial velocity is lower. The spread in C_{60} radius values is ± 0.025 Å, which is slightly higher than for the C_{60} in the (10, 10) tube. The (9, 9) tube radius changes are similar to that for the (10, 10) tube case.

For case 3, we applied an initial velocity from 400 to 1600 m/s to the C_{60} in the axial direction to see if it would enter the (8, 8), (7, 7), (6, 6), and (5, 5) tubes. For all these cases the C_{60} is not able to enter due to the strong repulsive action. Figures 7a−c show the typical response for the case of an (8, 8) tube with initial velocity of 800 m/s. There are also visible deformations for both the C_{60} and (8, 8) tube at the open tip. For a detailed description, animations are available on the web (http://tam.nwu.edu/wkl/c60_in_tube).

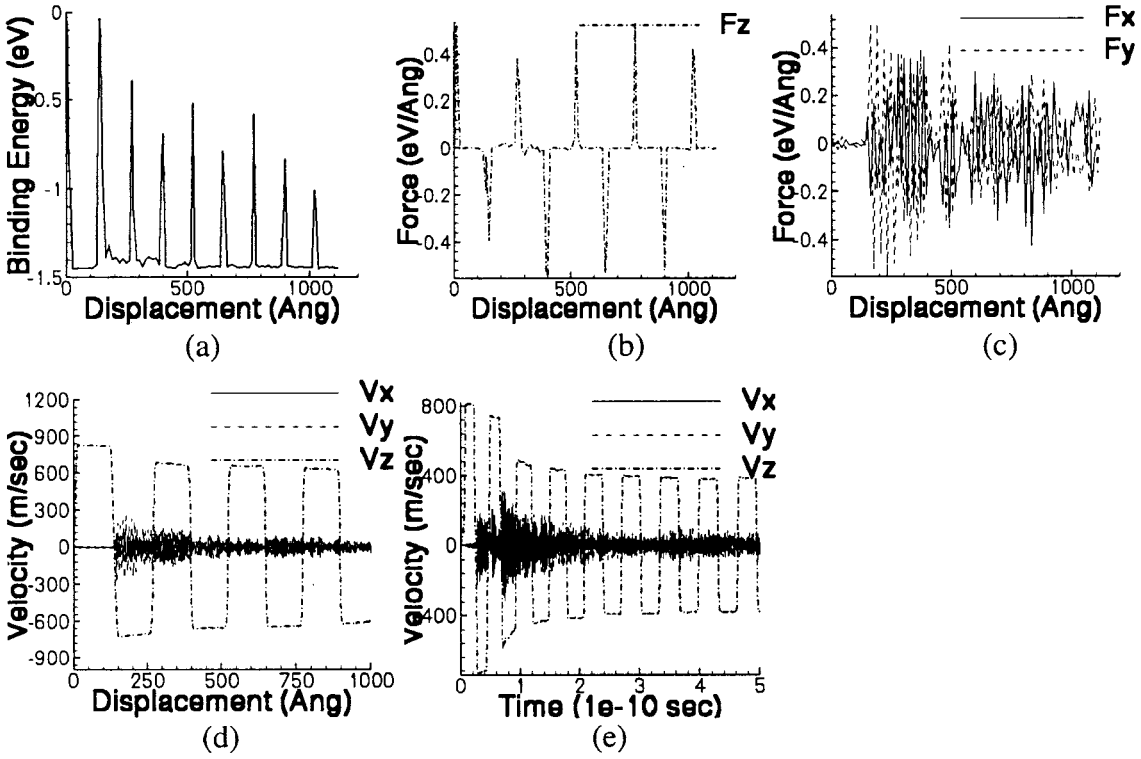

Figure 6. (a) Binding energy as a function of displacement for C_{60} traversing the (10, 10) nanotube eight times (back and forth, thus 4 full cycles). (b) The total axial force acting on the C_{60}. (c) The *x* and *y* components of the total force acting on the C_{60}. (d) The three velocity components of the C_{60}. (e) The history of the three velocity components of C_{60} as it traverses the (10, 10) nanotube twenty times.

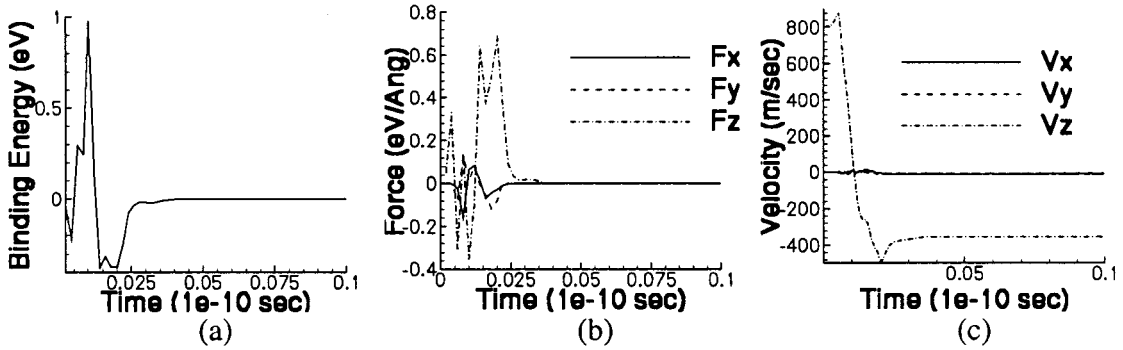

Figure 7. C_{60} fired at the (8,8) nanotube. (a) The binding energy history for the (8,8) nanotube. (b) The total axial force acting on the C_{60}. (c) The total force acting on the C_{60} in the *x* and *y* directions. (d) The velocity component of the C_{60} in the axial direction.

Conclusions and Remarks

A combined continuum/molecular dynamics approach for the analysis of interaction between C_{60} and 6 different armchair nanotubes is presented. This approach bridges the in-plane bonding as treated by the Tersoff-Brenner potential, with the continuum property of the material, which additionally serves as a useful tool for evaluating the bonding potentials. C_{60} is "sucked" into the (10, 10) or (9, 9) tube by the sharp surface tension force present in the front of the open end and then oscillates between the two open ends of the nanotube, never escaping. After stabilizing after a few cycles the oscillation shows little decay. Both the C_{60} molecule and the nanotube show small deformations as a function of time and position. C_{60}, even when fired on axis with an initial speed up to 1600m/s, cannot penetrate into the (8, 8), (7, 7), (6, 6), or (5, 5) nanotubes. The simulation results suggest the possibility of using C_{60} molecules in nanotubes for making nano-devices such as a nanobearing or nano-piston.

Acknowledgment. The work of Q.D. and W.K.L. is supported by grants from NSF and the Tull Family Endowment. R.S.R. appreciates support from the NASA Langley Research Center for Computational Materials: Nanotechnology Modeling and Simulation Program; and support to R.S.R. and W.K.L. from the ONR Miniaturized Intelligent Sensors Program is acknowledged..

References and Notes

(1) Smith, B. W.; Monthoux, M.; Luzzi, D. E. *Nature* **1998**, *336*, 323.

(2) Smith, B. W.; Monthoux, M.; Luzzi, D. E. *Chem. Phys. Lett.* **1999**, *315*, 31−36.

(3) Smith, B. W.; Luzzi, D. E. *Chem. Phys. Lett.* **2000**, *321*, 169−174.

(4) Burteaux, B.; Claye, A.; Smith, B. W.; Monthoux, M.; Luzzi, D. E.; Fischer, J. E. *Chem. Phys. Lett.* **1999**, *310*, 21−24.

(5) Sloan, J.; Dunin-Borkowski, R. E.; Hutchinson, J. L.; Coleman, K. S.; Williams, V. C.; Claridge, J. B.; York, A. E.; Bailey, S. R.; Brown, G.; Fridrichs, S.; Green, M. L. H. *Chem. Phys. Lett.* **2000**, *316*, 191−198.

(6) Zhang, Y.; Iijima, S.; Shi, Z.; Gu, Z. *Philos. Mag. Lett.* **1999**, *79*, 473−479.

(7) Sloan, J.; Hammer, J.; Zwiefka-Sibley, M.; Green, M. L. *Chem. Commun.* **1998**, *3*, 347−348.
(8) Yu, M. F.; Yakobson, B. I.; Ruoff, R. S. *J. Phys. Chem. B* **2000**, *104*, 8764.
(9) Cumings, J.; Zettl, A. *Science* **2000**, *289*, 602.
(10) Girifalcon, C. A.; Lad, R. A. J. *Chem. Phys.* **1956**, *25*, 693−697.
(11) Girifalco, C. A. *J. Phys. Chem.* **1992**, *96*, 858−861.
(12) Wang, Y.; Tomanek, D.; Bertsch, G. F. *Phys. Rev. B* **1991**, *44* (12), 6562−6565.
(13) Zhao, Y. X.; Spain, I. L. *Phys. Rev. B* **1989**, *40* (2), 993−997.
(14) Hanfland, M. *Phys. Rev. B* **1989**, *39* (17), 12598−12603.
(15) Boettger, J. C. *Phys. Rev. B* **1997**, *55* (17), 11202−11211.
(16) Tersoff, J. *Phys. Rev. B* **1989**, *39*, 5566.
(17) Brenner, D. W. *Phys. Rev. B* **1990**, *42*, 9458.
(18) Tadmor, E. B.; Ortiz, M.; Phillips, R. *Philos. Mag.* **1996**, *73* (6), 1529−1563.
(19) Milstein, F. In *Mechanics of Solids*; Hopkins, H. G., Sewell, M. J., Eds.; Pergamon Press: Oxford, 1982; pp 417−452.
(20) Belytschko, T.; Liu, W. K.; Moran, B. *Nonlinear finite elements for continua and structures*; John Wiley & Sons Ltd.: New York, 2000.
(21) Dresselhaus, M. S.; Dresselhaus, G.; Eklund, P. *Science of Fullerenes and Carbon Nanotubes*; Academic Press: New York, 1996.
(22) Liu, W. K.; Jun, S.; Zhang, Y. F. *Int. J. Numer. Methods Fluids* **1995**, *20*, 1081−1106.
(23) Qian, D.; Liu, W. K.; Ruoff, R. S. In process.
(24) Li, S.; Hao, W.; Liu, W. K. *Computational Mechanics* **2000**, *25*, 102−116.
(25) Liu, W. K.; Chen, Y.; Uras, R. A.; Chang, C. T. *Comput. Methods Appl. Mechanics Engineering* **1996**, *139*, 91−158.
(26) The two special journal issues are *Comput. Methods Appl. Mechanics Engineering* **1996**, *139*, and *Computational Mechanics* **2000**, *25*.